

Intensification of Large-Scale Stretching of Atmospheric Pollutant Clouds due to Climate Change

TÍMEA HASZPRA

*Institute for Theoretical Physics, and MTA-ELTE Theoretical Physics Research Group,
Eötvös Loránd University, Budapest, Hungary*

(Manuscript received 25 April 2017, in final form 28 September 2017)

ABSTRACT

The aim of the paper is to investigate the question of how a changing climate influences the spreading of pollutants on continental and global scales. For characterizing the spreading, a measure of chaotic systems, called topological entropy, is used. This quantity describes the exponential stretching of pollutant clouds and, therefore, is related to the predictability and the complexity of the structure of a pollutant cloud. For the dispersion simulations the ERA-Interim database is used from 1979 to 2015. The simulations demonstrate that during this period the mean topological entropy slightly increases: the length of an initially line-like pollutant cloud advected for 10 (30) days in the atmosphere becomes 20%–65% (200%–400%) longer by the 2010s than in the 1980s. The mean topological entropy is found to be strongly correlated with the mean of the absolute value of the relative vorticity and only weakly linked to the mean temperature.

1. Introduction


One of the most challenging problems of the present day is the assessment of the consequences of climate change, several of which are not yet explored satisfactorily. To the best of our knowledge, one aspect that has not been investigated yet is the impact of climate change on the large-scale atmospheric transport processes—that is, the investigation of the change in the characteristics of the spreading (e.g., speed and predictability, or the structure) of pollutant clouds.

Recently, two major events drew attention to the potentially important consequences of large-scale atmospheric transport: the ash plumes of the Eyjafjallajökull volcano's eruption in 2010, which resulted in airspace closures over Europe (e.g., [Flentje et al. 2010](#)), and the radioactive material released during the accident of the Fukushima Daiichi nuclear power plant, which caused measurable effects far away from the source, even in the United States and Europe (e.g., [Lujanienė et al. 2012](#); [MacMullin et al. 2012](#); [Mészáros et al. 2016](#)). Therefore, the investigation and modeling of the events

in which pollutants rise high in the atmosphere and may have continental and global impacts are particularly important.

Although there are studies dealing with the connection between climate change and air quality (e.g., [Bytnerowicz et al. 2007](#); [Kinney 2008](#)), these mainly focus on regional or local scales or the changes in pollutant concentration, rather than the transport itself ([Ma et al. 2004](#); [Jacob and Winner 2009](#); [Fang et al. 2011](#)). Thus, the purpose of this research is to fill the gap and carry out a detailed analysis to reveal whether the intensity of the large-scale transport processes is altered or not by the changing climate. In this paper, we focus on the past decades and investigate the instrumentally observed climate change ([IPCC 2013](#)) for the time period from 1979 to present. With the help of dispersion simulations based on atmospheric reanalysis data we are able to investigate a large number of events distributed uniformly in time and space, so that they are suitable for a statistical analysis to investigate whether the characteristics of atmospheric spreading are altered or not on a detectable level in the past 37 yr.

In the case of large-scale atmospheric dispersion, in which the characteristic time scale is on the order of 10 days, the typical horizontal distance of the transport of pollutants by the mean wind is on the order of 1000 km. Meanwhile, for the horizontal turbulent diffusion the characteristic length scale is about 3–30 km ([Haszpra and Tél 2013b](#)). Therefore, as a first approximation,

 Denotes content that is immediately available upon publication as open access.

Corresponding author: Tímea Haszpra, hatimi@caesar.elte.hu

DOI: 10.1175/JAS-D-17-0133.1

© 2017 American Meteorological Society. For information regarding reuse of this content and general copyright information, consult the [AMS Copyright Policy](#) (www.ametsoc.org/PUBSReuseLicenses).

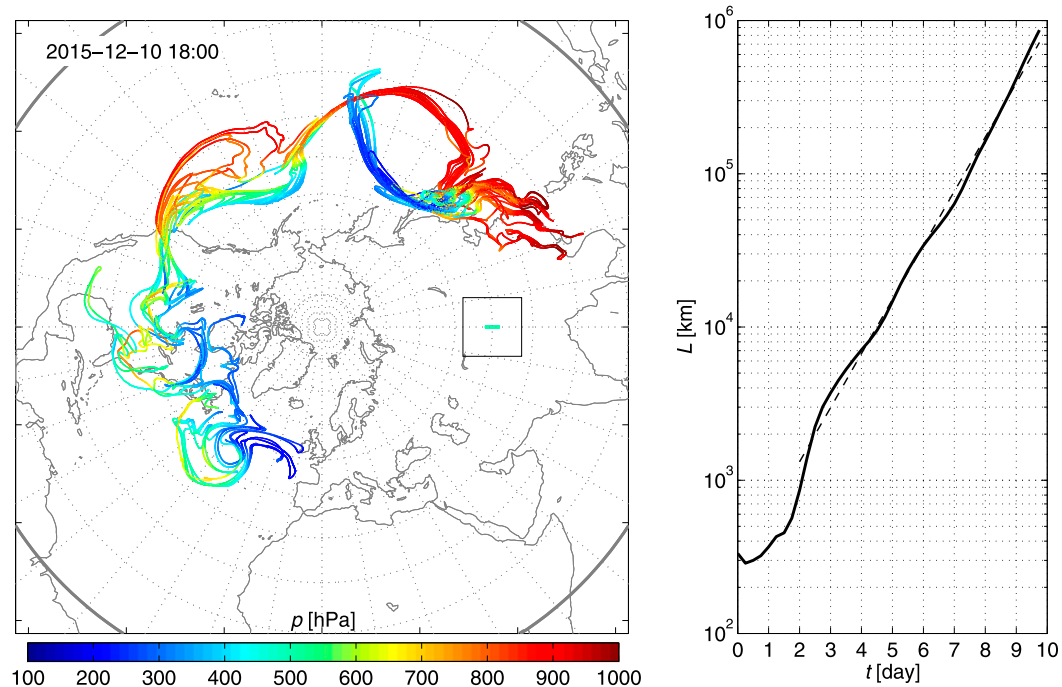


FIG. 1. (left) Advection image of a 3° -long line segment ($n_0 = 1000$ particles, initiated at 0000 UTC 1 Dec 2015 at 40°N , 90°E at 500 hPa) on the tenth day after the emission. Color bar indicates the pressure coordinate (hPa) of the particles. The initial position of the line segment is marked by the green line surrounded by the black square. (right) The length of the filament in time [solid line, determined as in Eq. (4)] and the fitted exponential function (dashed line) with exponent $h = 0.81 \text{ day}^{-1}$.

the stochastic part of the dispersion, that is, the effect of turbulent diffusion, can be neglected in the calculation of the transport of the pollutants. In this study, we consider the pollutant to be an inert gas. Because most of the time the pollutants are transported in the free atmosphere, deposition processes do not have a significant role. Hence, the transport of the pollutant is determined only by the advection process, which is deterministic. In the particle-tracking method applied in this study, the motion of a particle is described by three time-dependent, deterministic ordinary differential equations. In a dynamical system described by such a set of equations, chaotic behavior can occur; that is, the dynamics can be sensitive to the initial conditions, making it unpredictable for an extended time (Ottino 1989; Ott 2002).

To analyze the impact of a changing climate on the large-scale transport processes, we use a measure of chaos called the topological entropy (Newhouse and Pignataro 1993; Ott 2002; Tél and Gruiz 2006). In the context of large-scale transport, topological entropy describes the stretching rate of the pollutant clouds. As a measure of folding, it also describes the complexity of the structure of the pollutant cloud and the intensity and predictability of the spreading of the pollutant. As a rule of thumb, a larger value of the topological entropy implies the coverage of a larger geographical area by

pollutants (Haszpra and Tél 2013b). A pollutant cloud typically spreads in the atmosphere in a folded, filamentary structure as illustrated by Fig. 1. The figure shows the advection pattern of a pollutant cloud that consists of a large number of tracer particles, which form a 3° -long line segment on the 500-hPa level at the beginning of the simulation (see the green line within the black square). One can see that within 10 days the filament becomes highly stretched and folded as a result of the shearing and mixing effects of the atmospheric flow and covers a large part of the hemisphere. It is worth noting that the effects of two cyclones are noticeable in the lower-left part of the left panel. These cyclones force the pollutant particles to converge toward their centers by forming spirals and lift the particles high (marked by dark blue) in the atmosphere.

If the pollutant clouds are initialized as line segments, the length L of the filaments typically increases exponentially over time t :

$$L \sim \exp(ht), \quad (1)$$

where the exponent h denotes the topological entropy, that is, the stretching rate. This process is illustrated by the right panel of Fig. 1, in which the fitted exponential

function from day 2 to day 10 is marked by the dashed line. The length of the filament increases by a factor of about 3000 during the investigated time period. Note that a line segment cannot split up into two or more branches, because it would require a wind vector that points in more than one direction at some location. As a consequence, a line segment remains a line segment forever, and the determination of the full (folded) length is unambiguous. For more details on the topological entropy, see, for example, Thiffeault (2010); Budišić and Thiffeault (2015), and Haszpra and Tél (2013b) in the atmospheric context.

At the mid- and high latitudes, the characteristic values of h are found to be $0.6\text{--}0.8\text{day}^{-1}$, which indicates a stretching of the filaments by a factor of 400–3000 within 10 days. The stretching rate of pollutant clouds is dependent on the season (Haszpra and Tél 2013b). Therefore, it is plausible to assume that it also depends on the changing state of the climate. As the stretching rate is the exponent that describes the exponential growth, small deviations in its value result in significant differences in the length of the expanding clouds. For example, the slight increase of $10^{-3}\text{day}^{-1}\text{yr}^{-1}$ in the stretching rate over 37 yr would result in a change of about 50% and 300% increase of the length after 10 days and a month, respectively.

The paper is organized as follows. Section 2 provides a brief overview of the Real Particle Lagrangian Trajectory (RePLaT) model (Haszpra and Tél 2013a; Haszpra and Horányi 2014) and the equations of motion by which the trajectories of the pollutant particles that form the pollutant clouds are determined. It also includes the description of the meteorological data and the initial setup of the simulations. The results are presented in section 3, and section 4 summarizes the main conclusions of the work.

2. Equations, data, and methods

For the simulation of the spreading of the atmospheric pollutant clouds the RePLaT atmospheric dispersion model is used. RePLaT is a Lagrangian trajectory model that tracks individual spherical particles with fixed, realistic radius and density. The velocity is given by the Newtonian equation of motion of a finite-size particle in a prescribed wind field, and in the vertical direction deposition is also taken into account. RePLaT can reckon with the effect of turbulent diffusion on the particles as a stochastic term in the equations of motion, and it can simulate the scavenging of particles by precipitation as a random process that results in a particle being captured by a raindrop with a probability depending on the precipitation intensity and the collision efficiency of

raindrops and aerosol particles. RePLaT was tested by simulating the dispersion of volcanic ash from volcanic eruptions such as the ones of Eyjafjallajökull and Mount Merapi (Haszpra and Tél 2011, 2013a) and by simulating the dispersion and deposition of the radioactive particles released during the accident of the Fukushima Daiichi nuclear power plant (Haszpra and Tél 2016). In the former studies reasonable agreement was found between the distribution of volcanic ash in the simulation and that indicated by satellite measurements. In the case of the Fukushima Daiichi accident the arrival times of the pollution at different locations coincided with the observation, and the simulations were able to reproduce the measured concentrations of the noble gas ^{133}Xe with acceptable accuracy.

In this paper, the calculation of the particle trajectories are carried out with the simplest configuration, in which only advection is considered. In the simulations, ideal tracers, corresponding to inert gases or infinitesimally small air parcels, are tracked. In this case, the velocity \mathbf{v}_p of a particle equals to the velocity \mathbf{v} of the wind at the location \mathbf{r}_p of the particle at time t , and the equation of motion of the particles is

$$\dot{\mathbf{r}}_p(t) \equiv \mathbf{v}_p(t) = \mathbf{v}[\mathbf{r}_p(t), t]. \quad (2)$$

In the present study, if a tracer particle encounters with the surface, it bounces back to the atmosphere by a perfectly elastic collision. RePLaT determines the particle trajectories in longitude–latitude–pressure coordinate system using Euler’s method, that is, the position \mathbf{r}_p of a particle at time $t + \Delta t$ is calculated as

$$\mathbf{r}_p(t + \Delta t) = \mathbf{r}_p(t) + \mathbf{v}[\mathbf{r}_p(t), t]\Delta t. \quad (3)$$

The meteorological data required for the trajectory calculation, that is, the wind field with zonal u , meridional v , and vertical ω velocity components in pressure coordinates [$\mathbf{v} = (u, v, \omega)$], as well as variables necessary for analyzing the climatic impact [e.g., the temperature fields T , geopotential fields Φ , and potential vorticity fields (PV)], are ERA-Interim data from the European Centre for Medium-Range Weather Forecasts (ECMWF) (Dee et al. 2011) on a $1.5^\circ \times 1.5^\circ$ horizontal grid with 6-h time resolution. The time step we use in RePLaT in this study is the same $\Delta t = 45$ min as in Haszpra and Tél (2013b), as it proved to be sufficiently small for free-atmospheric transport simulations.

For the computation of the topological entropy (stretching rate) we take line segments of initial length of $3^\circ \approx 330$ km at $p_0 = 500$ hPa in the free atmosphere that consist of $n = 10^3$ uniformly distributed ideal particles and we track these degenerate “pollutant clouds”

for 10 days. When the distance of two neighboring particles exceeds 10 km, a new particle is inserted between them. Owing to the exponential stretching of a line segment, the number of particles in the simulations increases (not uniformly along the filament) and can reach $n = 10^6$ after 10 days, while its average is on the order of 10^4 . To gain a global picture, 12×17 meridional line segments are located on a geographical grid over the globe from $\lambda_0 = 150^\circ\text{W}$ to 180° in increments of 30° and from $\varphi_0 = 80^\circ\text{S}$ to 80°N in increments of 10° .

The length of a filament at time t is calculated by the sum of the distances between its particles:

$$L(t) = \sum_{i=1}^{n-1} |\mathbf{r}_{p,i}(t) - \mathbf{r}_{p,i+1}(t)|, \quad (4)$$

where $\mathbf{r}_{p,i}$ is the position of the i th particle. Since vertical stretching proved to be 10^{-2} – 10^{-3} times smaller than the horizontal one in our previous study (Haszpra and Tél 2013b), we also neglect it in this paper. Thus, the length of a filament is obtained from the horizontal distances between particle pairs, and the distance (km) is calculated along great circles by

$$\begin{aligned} |\mathbf{r}_{p,i}(t) - \mathbf{r}_{p,i+1}(t)| &= \arccos[\sin\varphi_{p,i} \sin\varphi_{p,i+1} \\ &\quad + \cos\varphi_{p,i} \cos\varphi_{p,i+1} \cos(\lambda_{p,i} - \lambda_{p,i+1})] \\ &\quad \times \frac{180}{\pi} \times 111.1, \end{aligned} \quad (5)$$

where $\lambda_{p,i}$ and $\varphi_{p,i}$ are the longitudinal and latitudinal coordinate of the i th particle, respectively, and $(180/\pi) \times 111.1$ converts the unit from radians to kilometers using the fact that the spherical distance of 1° along a great circle corresponds to a length of 111.1 km along the surface. The filaments are tracked for a 10-day-long time period, characteristic to continental and global transport processes. It is worth noting that tracking the particles for a much longer time could result in smaller geographical differences in the topological entropy, because line segments of the mid- and high latitudes are mixing in the hemisphere rapidly and may cover almost a whole hemisphere within about a month (Haszpra and Tél 2013b).

3. Results

a. Time evolution of the stretching rate due to climate change

To find a relationship between changing climate conditions and the characteristics of the spreading, and to study the possible seasonal effects, we run dispersion simulations with the RePLaT model for each year from 1979 to 2015 for the December–February (DJF)

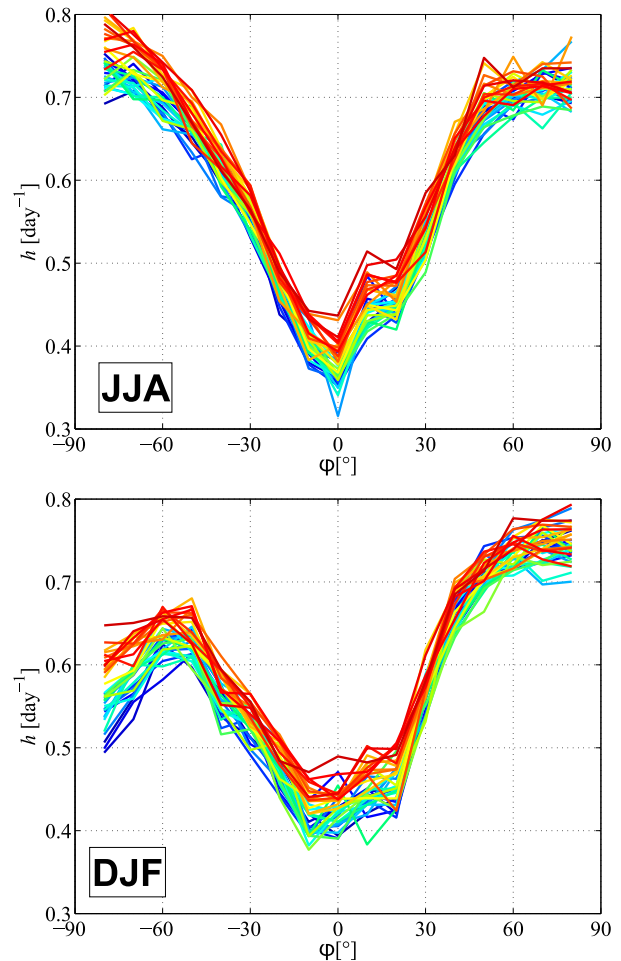


FIG. 2. The zonal and seasonal means of the stretching rate h in (top) JJA and (bottom) DJF from 1979 to 2015. Each line connects the mean of the different latitudes for a given year. Lines are colored from blue to red from 1979 to 2015.

and June–August (JJA) seasons. The line segments introduced in section 2 are generated every 10 days and tracked for 10-day periods. The length of the line segments is computed at each time instant and an exponential function is fitted to the resulting data from day 2 to day 10 to obtain an estimate of the value of the stretching rate h .

Figure 2 illustrates the zonal- and seasonal-mean values of the stretching rate from 1979 to 2015 during JJA and DJF. The curves for the later years, which are marked by warmer colors, have generally somewhat higher values at each latitude. The values for the different years range from 0.05 to 0.15 day^{-1} over the globe. The distribution of the zonal-mean stretching rate, that is, the shape of the curves, does not change significantly over the 37 yr. One can also notice that in each year larger values characterize the mid- and high

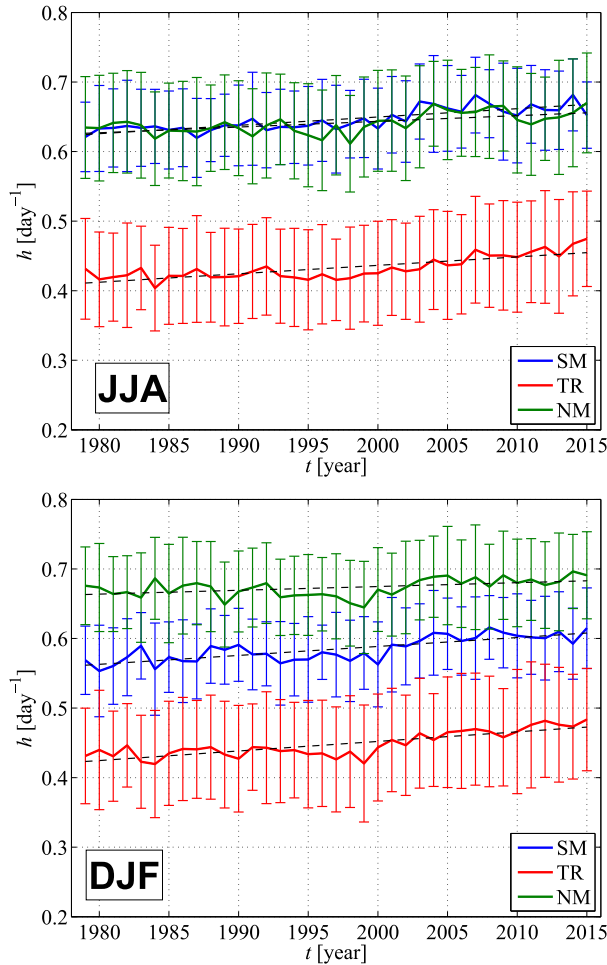


FIG. 3. The regional and seasonal means of the stretching rate h with the standard deviation of the seasonal-mean values for TR, NM, and SM in (top) JJA and (bottom) DJF from 1979 to 2015. Dashed lines denote linear fits to the data with slopes in Table 1.

latitudes ($0.5\text{--}0.8\text{ day}^{-1}$), where more intense cyclonic activity takes place than in the tropical belt ($0.3\text{--}0.5\text{ day}^{-1}$), in all years. To demonstrate the large difference between the stretching rates of the different regions, it is useful to consider a characteristic value of 0.7 day^{-1} for the extratropics and 0.4 day^{-1} for the tropics: they result in a length increase of a factor of 1100 and 55 over 10 days, respectively; that is, an almost twice-as-large stretching rate is associated with an ~ 20 -times-longer filament. Both hemispheres have the maximum values in their respective winter season, in which the circulation is more active than in the summer season. The average difference between the winter and summer seasons is greater for the Southern Hemisphere (SH) than for the Northern Hemisphere (NH), which might be the consequence of the larger portion of oceanic regions, which reduces the impact of lands on the wind.

TABLE 1. The slopes of the curves in Fig. 3 ($10^{-1}\text{ day}^{-1}\text{ yr}^{-1}$) with 95% confidence intervals.

	SM	TR	NM
JJA	1.199 ± 0.303	1.214 ± 0.326	0.818 ± 0.367
DJF	1.285 ± 0.343	1.376 ± 0.330	0.546 ± 0.356

To provide further support to our initial conclusion about the increasing stretching rate values for the time period 1979–2015, Fig. 3 presents the time evolution of the areal mean of the stretching rate for 1979–2015 for different geographical regions: tropics (TR; $\varphi_0 = 20^\circ\text{S}\text{--}20^\circ\text{N}$), NH extratropics (NM; $\varphi_0 = 30^\circ\text{--}80^\circ\text{N}$), and SH extratropics (SM; $\varphi_0 = 30^\circ\text{--}80^\circ\text{S}$). Dashed lines indicate linear fits to the data, and their slopes are given in Table 1. The figure and the table show a slow, but definite, increase of the mean values of the stretching rates from 1979 to 2015, with fluctuations that are an order of magnitude smaller. The largest change is in the tropics, while the smallest one is in the NH extratropics. For example, the increase of the stretching rate from about 0.42 to 0.47 day^{-1} in the tropics in DJF implies an increase of the length of the 10-day-old filaments by a factor of about $\exp(0.47\text{ day}^{-1} \times 10\text{ day}) / \exp(0.42\text{ day}^{-1} \times 10\text{ day}) = \exp(0.5) \approx 1.65$. The same factor for the NH extratropics in DJF, where the stretching rate increases from about 0.62 to 0.64 day^{-1} , is 1.22. A formal extrapolation of the results for a 30-day period would suggest that the length of the filaments advected in the atmosphere for a month can be 4.5 times larger in the 2010s than in the 1980s in the tropics and SH extratropics and 1.82 times larger in the NH extratropics. Obviously, filaments that originate in the tropics usually mix into the midlatitudinal atmospheric circulation within 30 days, and vice versa, the filaments that originate in the extratropics can mix into the tropics. Therefore the true mean stretching rates and length factors lie between the values obtained by extrapolation, assuming a complete separation of the regions.

It is worth noting that while the order of magnitude of the mean values is 10^{-1} day^{-1} , the increase of the stretching rate is on the order of $10^{-4}\text{--}10^{-3}\text{ day}^{-1}\text{ yr}^{-1}$, which represents a yearly increment on the order of magnitude 2–3 times smaller than the mean values. These values underline the fact that even the apparently small increase in the stretching rate during the past four decades leads to 20%–65% (200%–400%) longer pollutant filaments after a 10 (30)-day advection. The importance of this result lies in the fact that it suggests that radioactive pollutants or pollutants from volcanic eruptions could reach a significantly larger region in the 2010s than in the 1980s.

b. Relation to meteorological quantities

Our next step is to find a relationship between the time evolution of the stretching rate and different meteorological variables. Finding a connection between the Lagrangian characteristics of the spreading of pollutants and the Eulerian features of climate would be useful in situations where the properties of the spreading would have to be estimated for a different climate, as it would not require a large number of computationally costly extra dispersion simulations.

Because the stretching rate is calculated from particle positions, it is a Lagrangian quantity. Thus, one cannot expect to find an exact link between its behavior and the Eulerian meteorological fields unless the meteorological data are considered along the particle trajectories of the filaments. In the hope that an estimate of the change of the stretching rate can be obtained by utilizing only Eulerian information about the meteorological fields, without making transport simulations, we compare areal averages of the Eulerian meteorological fields for fixed regions (atmospheric volumes) with Eulerian fields of the mean stretching rate of pollutant clouds in the SM, TR, and NM region, rather than averaging over the grid cells covered by the particles, since the latter would only characterize a particular pollutant cloud, while the former is of regional relevance. As Fig. 1 illustrates, a filament that is initialized as a few-hundred-kilometer-long line segment often covers a significant region of a hemisphere after 10 days, and it rarely mixes into the other hemisphere within that time. Therefore, we select the latitudinal boundaries of the “boxes” (atmospheric volumes) for the predictions of the mean stretching rate of SM, TR, and NM to be 90°S – 0° , 45°S – 45°N , and 0° – 90°N , respectively. Motivated by the vertical extent of the evolved line segment in Fig. 1, the boundaries of the pressure levels have been chosen as 1000 and 100 hPa. In addition, the effect of considering single levels (300, 500, and 850 hPa and 315 and 330 K) has been also analyzed.

Based on Eqs. (2) and (4), the stretching rate is fully determined by the wind field, and the stretching of a line segment can be linked to the spatial inhomogeneity of the velocity values along the filament (i.e., derivatives of the wind speed). Therefore, as a first step, we investigate the relationship with the relative vorticity and shear stress. As climate change is mostly interpreted in terms of temperature change, the potential connection between the stretching rate and temperature, as well as the equator-to-pole temperature difference, is also analyzed at different atmospheric levels. Besides these, we also investigate other meteorological variables, such as potential vorticity and geopotential heights, which are

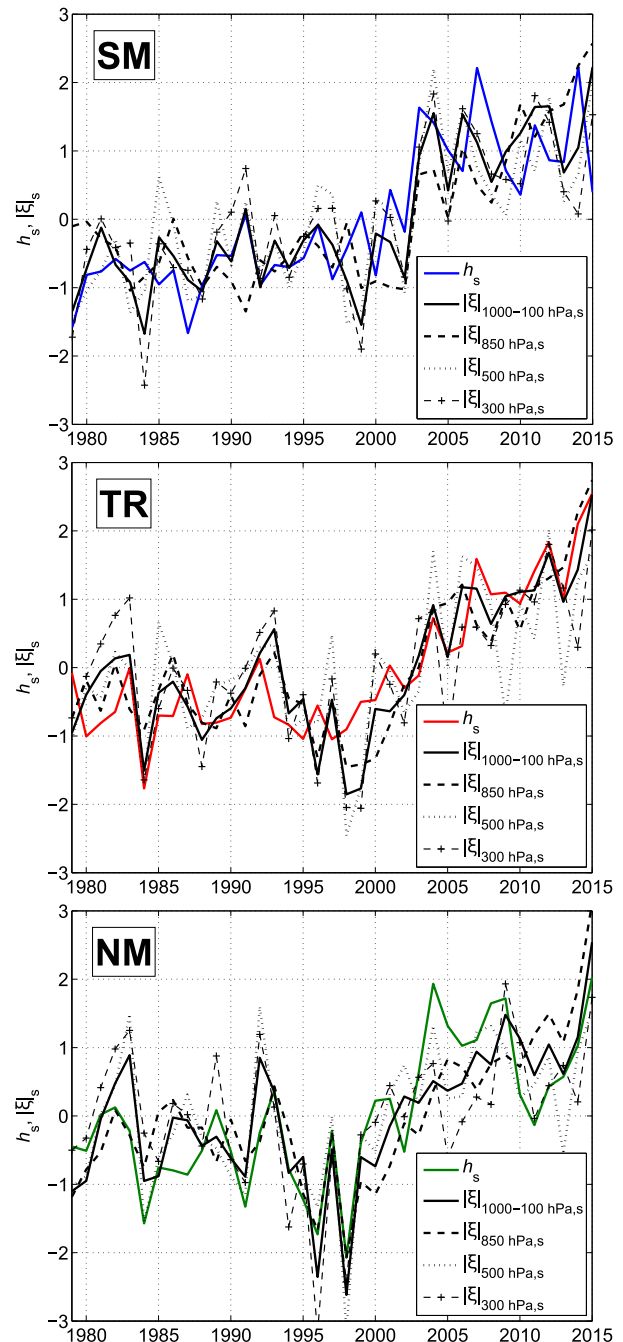


FIG. 4. The time evolution of the mean stretching rate h_s and the mean of the absolute value of the relative vorticity $|\xi|_s$, both standardized over time, for different pressure levels in JJA for (top) TR, (middle) NM, and (bottom) SM.

often used for the identification of synoptic-scale weather systems, and horizontal wind speed and kinetic energy, to provide a more comprehensive view of variables possibly influencing the evolution of the stretching rate.

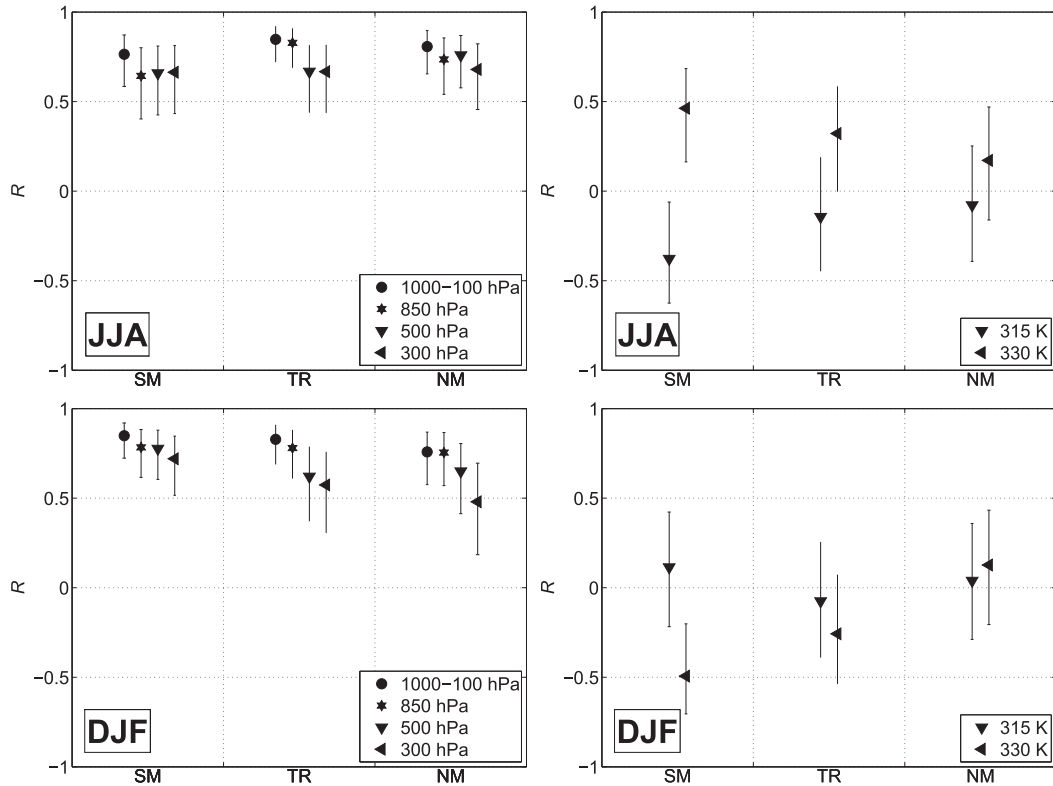


FIG. 5. The correlation coefficient R of the mean stretching rate with (left) the mean of the absolute value of the relative vorticity for different pressure levels and (right) the mean of the absolute value of the potential vorticity anomaly for different isentropic levels with 95% confidence intervals in (top) JJA and (bottom) DJF for TR, NM, and SM.

As an illustration, Fig. 4 presents the time evolution of the mean stretching rate and the mean of the absolute value of the relative vorticity, both standardized over time for illustrative purposes, at the chosen pressure levels for SM, TR, and NM in JJA. (Standardized quantities for the time series of a general scalar state variable q are calculated as $q_s = (q - \bar{q})/\sigma_q$, where \bar{q} is the temporal mean value of q and σ_q is the standard deviation of q over the investigated time interval.) The two quantities are apparently not independent of each other: usually the increase (decrease) in relative vorticity is associated with the increase (decrease) in stretching rate. To be more quantitative, the left panels of Fig. 5 show the correlation coefficients for the time series of the two quantities. In all of the three regions the correlations are statistically significant at the 95% level. The strongest correlations exceed 0.8 and are related to averages taken through the entire depth of the 1000–100 hPa layer of the atmosphere. Note that considering only the data at the 300-, 500-, or 850-hPa level gives a correlation coefficient above 0.6 as well. The statistics for the shear stress behaves similarly (not shown). This confirms our expectation that there exists a relation between the stretching rate of the

pollutant line segments and the absolute value of the relative vorticity/shear stress.

Based on the results of relative vorticity, it seems to be useful to investigate the relationship of the stretching rate with potential vorticity, which is often applied in the investigation of the dynamics of cyclones (e.g., Davis and Emanuel 1991; Stoelinga 1996; Möller and Montgomery 2000). Ertel potential vorticity is given by $PV = -g(\xi_\theta + f)\partial\theta/\partial p$, where g is the gravitational acceleration, ξ_θ is the relative isentropic vorticity, f is the Coriolis parameter, θ is the potential temperature, and p is the pressure. That is, PV is the product of the absolute vorticity and the static stability, therefore, consists of a dynamical factor and a thermodynamic factor. While positive potential anomaly implies large cyclonic absolute vorticity and/or stronger stability, negative anomaly is associated with large anticyclonic absolute vorticity and/or weaker static stability. In this paper the reference state for the calculation of anomalies is chosen as in Van Delden and Hinszen (2012): $PV_{ref} = f/(-\partial\theta/\partial p)_{ref}$, where $(-\partial\theta/\partial p)_{ref}$ (the reference isentropic density) is determined for one hemisphere as the horizontal average of $(-\partial\theta/\partial p)$ from latitude 10° to 90° . We investigate

TABLE 2. The correlation coefficient R of the mean stretching rate and the mean of the geopotential height Φ , wind speed $|\mathbf{v}|$, kinetic energy (KE), and equator-to-pole temperature difference ΔT_{2m} , for raw and detrended data, in JJA and DJF for TR, NM, and SM. Values statistically significant at the 95% level are marked by an asterisk.

			Raw			Detrended		
			SM	TR	NM	SM	TR	NM
Φ	JJA	850 hPa	0.41*	0.12	0.07	0.03	-0.09	-0.09
		500 hPa	0.47*	0.42*	0.31*	0.07	0.13	-0.09
		300 hPa	0.56*	0.51*	0.32*	0.05	0.16	-0.10
	DJF	850 hPa	-0.16	0.21	0.20	-0.08	-0.10	-0.17
		500 hPa	0.08	0.44*	0.37*	0.06	0.07	0.04
		300 hPa	0.33*	0.52*	0.39*	0.05	0.09	0.09
$ \mathbf{v} $	JJA	1000-100 hPa	0.30	0.28	0.20	-0.03	0.20	0.24
		850 hPa	0.58*	0.68*	0.40*	0.06	0.21	0.08
		500 hPa	0.16	0.07	0.14	0.00	0.07	0.23
	DJF	300 hPa	0.00	-0.11	-0.17	-0.10	0.12	0.16
		1000-100 hPa	0.73*	0.32	0.49*	0.19	0.31	0.57*
		850 hPa	0.66*	0.76*	0.35*	0.11	0.48*	0.15
KE	JJA	500 hPa	0.62*	0.03	0.31	0.16	0.19	0.53*
		300 hPa	0.52*	0.05	0.27	0.11	0.21	0.43*
		1000-100 hPa	0.03	-0.05	-0.09	-0.12	0.10	0.20
	DJF	850 hPa	0.41*	0.55*	0.25	-0.05	0.12	0.01
		500 hPa	-0.05	-0.26	-0.17	-0.15	-0.09	0.13
		300 hPa	-0.14	-0.23	-0.26	-0.016	0.05	0.20
ΔT_{2m}	JJA	2 m	0.57*	0.11	0.30	0.01	0.23	0.40*
	DJF	850 hPa	0.61*	0.62*	0.17	0.02	0.42*	0.04
		500 hPa	0.47*	-0.08	0.12	-0.08	0.18	0.40*
		300 hPa	0.38*	-0.04	0.20	0.01	0.21	0.38*
		2 m	-0.03	—	-0.20	-0.18	—	0.14
		2 m	0.35*	—	-0.52*	-0.32	—	-0.29

the potential vorticity anomaly on two of the often used atmospheric levels in synoptic analysis, on the 315- and 330-K levels. The right column of Fig. 5 illustrates the correlation coefficients of the stretching rate with the absolute value of the potential vorticity anomaly. We find that, in contrast to the relative vorticity, the correlation coefficients for the potential vorticity anomaly considerably differ on different levels and can be both negative and positive at any given level.

The results related to the geopotential heights, wind speed, and kinetic energy are displayed in Table 2. The correlation coefficients are in general lower than those for the absolute value of the relative vorticity and some of them are nearly zero. The correlation coefficients for the wind speed and kinetic energy confirm the expectation that the stretching is related to the velocity differences along the advected line segment rather than to the velocity values themselves. The correlation of the geopotential height with the stretching rate is the strongest at the 300-hPa level and significant at the 95% level in almost all of the three regions in both seasons.

We repeated our calculations also for the 2-m temperature T_{2m} and the temperature T at selected pressure levels. Figure 6 is the analog of Fig. 4: it shows the time series of the mean stretching rate and the mean

temperatures, both standardized over time. The correlations for these variables are weaker than for the relative vorticity, but they generally change in the same (positive) direction with time. The corresponding correlation coefficients are displayed in Fig. 7. The correlation coefficients are the largest in the tropics. In JJA in TR and NM the temperatures of the lower and upper troposphere (i.e., T_{2m} , T_{850hPa} , and T_{300hPa}) are the most closely related to the stretching rate, while in DJF the strength of the relationship is similar for all of the altitudes investigated here. For SM the correlation coefficient for the 850-hPa level is small in both seasons.¹

As the equator-to-pole temperature difference is the driving force of the atmospheric circulation, we also investigate the relation between the stretching rate and ΔT_{2m} (Table 2). In JJA the correlation coefficients for SM and NM are found to be negative, falling below -0.2 and are statistically not significant at the 95% level. In

¹ This might be explained by the fact that because of Antarctica's high orography the particles in this hemisphere cannot stay in the lower (higher pressure) layers of the atmosphere in this extended region. While reanalysis data are available for the lower (higher pressure) levels like 1000 and 850 hPa, these levels are often subterraneous.

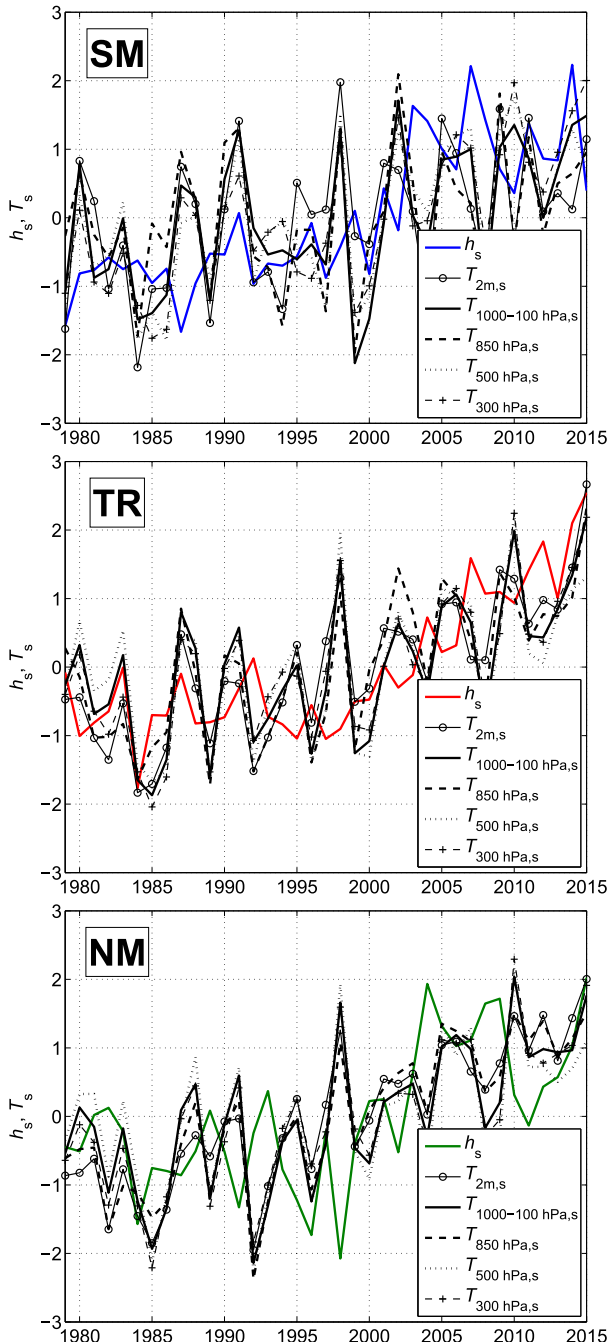


FIG. 6. The time evolution of the mean stretching rate h_s and the mean temperature T_s , both standardized over time, for different pressure levels in JJA for (top) SM, (middle) TR, and (bottom) NM.

contrast to JJA, in DJF the corresponding correlation coefficients are significant and have the opposite signs: 0.35 and -0.51 for SM and NM, respectively. This might be the consequence of the observed difference in the trends: an increasing ΔT_{2m} in the Southern Hemisphere, but a decreasing ΔT_{2m} in the Northern Hemisphere.

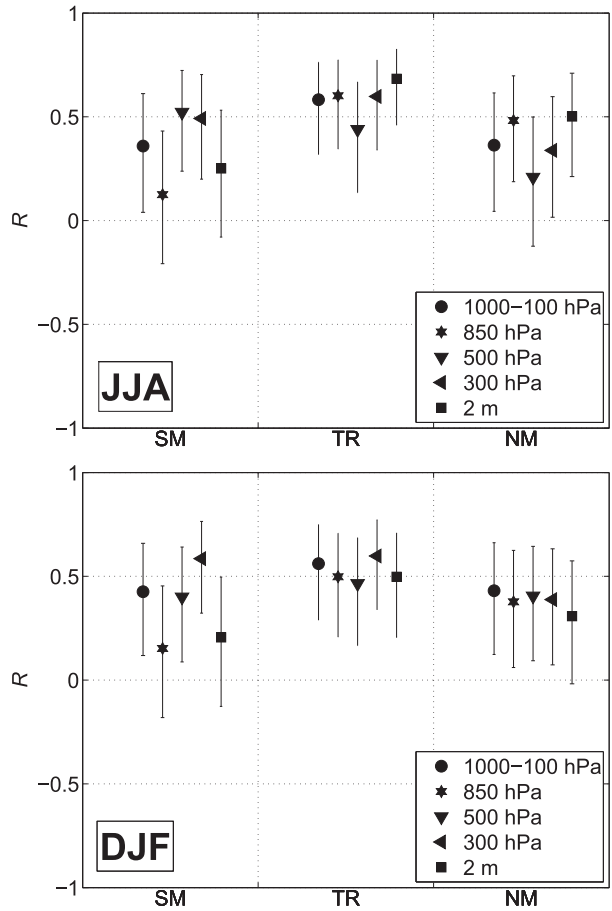


FIG. 7. The correlation coefficient R of the mean stretching rate and the mean temperature with 95% confidence intervals for different levels in (top) JJA and (bottom) DJF for TR, NM, and SM.

The change in the stretching rate of pollutant clouds is influenced by atmospheric structures like cyclones. More frequent or more intense cyclones imply a higher mean of the absolute value of the relative vorticity and the wind shear values and, therefore, an easier stretching of the pollutant filaments. Different reanalysis datasets provide slightly different, but correlated, results concerning the changes in cyclone properties (e.g., [Tilina et al. 2013](#); [Kelemen et al. 2015](#)). Although previous studies on the trends in the number and intensity of extratropical cyclones reported trends of different signs depending on the geographical location (e.g., [Gulev et al. 2001](#); [Graham and Diaz 2001](#); [Fyfe 2003](#); [Wang et al. 2006](#); [Ulbrich et al. 2009](#); [Wang et al. 2013](#)), the more recent studies concluded that the cyclonic activity increased since the 1980s in both hemispheres ([Tilina et al. 2013](#); [Wang et al. 2013](#)). Most of the papers suggest decreasing trends in the midlatitudes of both hemispheres and increasing trends in the high latitudes ([Serreze et al. 1997](#); [McCabe et al. 2001](#); [Geng and Sugi](#)

2001; Lim and Simmonds 2007, 2009; Ulbrich et al. 2009; Wang et al. 2013).

The overall increase of cyclonic activity is in agreement with our findings of positive trends in the stretching rates. Our results concerning the weaker link between the stretching rate of pollutant clouds and the mean temperature are in accordance with the findings of previous studies, in which cyclone frequency was found to be weakly correlated with the mean temperature (Agee 1991; Serreze et al. 1997; McCabe et al. 2001). The result that the mean stretching rate increases in both hemispheres—despite the opposite trend of ΔT_{2m} —may be explained by the fact that the effect of the change in the meridional temperature difference is complex and has diversified impacts (Hassanzadeh et al. 2014).

The correlation analysis hitherto described revealed that for most of the investigated quantities the mean values change similarly. To check if the shifts of the mean values due to climate change influence the correlations, we repeat the correlation analysis for the time series of the quantities after removing a linear trend. As expected based on Fig. 4, we find a relatively strong connection between the fluctuations of the absolute value of the relative vorticity and the stretching rate. Figure 8 shows that in almost all cases, the correlation coefficient is above 0.4 and can reach as high a value as 0.7. The correlation coefficients between the detrended temperature and stretching rates are below 0.3 and can even become slightly negative (not shown). The correlation coefficients for the remaining quantities are determined in the same way. The last three columns of Table 2 show that none of these quantities are as strongly correlated with the stretching rate as the relative vorticity. To conclude, this new analysis provides further evidence that the intensity of the stretching of the pollutant clouds and the complexity of their evolving structure are most closely related to the relative vorticity field.

4. Summary

For a simple characterization of the large-scale spreading of pollutant clouds, a quantity called topological entropy and well known in dynamical systems theory is used. In this particular context, the topological entropy is the rate of the exponential stretching of filament-like pollutant clouds. As a measure of folding, it is also closely related to the complexity and predictability of the pollutant clouds. In the tropics, pollutant line segments stretch by a factor of 20–150 within 10 days, while in the mid- and high latitudes the characteristic values of length increase are between 300 and 3000.

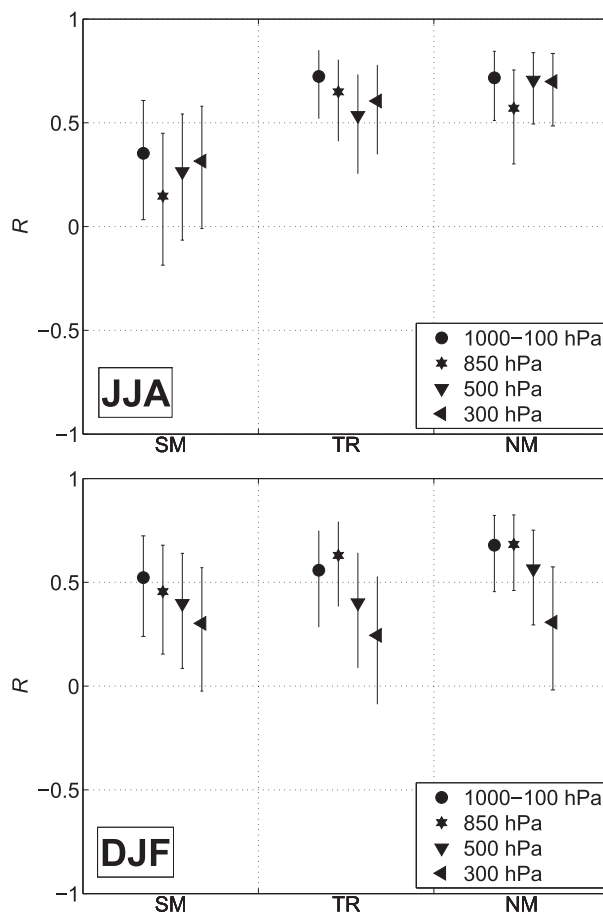


FIG. 8. The correlation coefficient R of the detrended mean stretching rate and the detrended mean of the absolute value of the relative vorticity with 95% confidence intervals for different levels in (top) JJA and (bottom) DJF for TR, NM, and SM.

We found a slight increase (3%–10%) in the values of the mean stretching rates in the three studied geographical regions (tropics and SH and NH extratropics) from 1979 to 2015. This increase of the mean stretching rate is equivalent to an increase of the characteristic length of the filaments by a factor of 1.2–1.65 over a period of 10 days. Larger stretching rate values indicate a more intense spreading, more foldings, and a larger geographical area covered by the pollutants. The increased mean stretching rate of the analyzed decades, therefore, implies the risk of a larger polluted region from a particular pollution event.

Finding a relationship between the stretching rate and the meteorological variables could help estimate the changes of large-scale transport properties of the atmosphere for the different climate projections without the necessity to carry out computationally costly extra transport simulations. For example, one would naively think that there is a definite connection between the

meridional temperature difference and the intensity of spreading (characterized by the stretching rate), but the analyzed data do not support this assumption. We found that the areal mean of the absolute value of the relative vorticity for the atmospheric layer between 1000 and 100 hPa, or for a single pressure level in the free atmosphere, is well correlated with the stretching rate. This correlation is much stronger than those for the temperature, geopotential height, wind speed, kinetic energy, and potential vorticity.

Acknowledgments. The author thanks the useful discussions with and suggestions of G. Drótos, T. Tél, and A. Várai. P. Csomós, M. Herein, M. Vincze, and T. Weidinger are also acknowledged for valuable comments and remarks. The author thanks one of the anonymous referees for the suggestions on wording. This paper was supported by the János Bolyai Research Scholarship of the Hungarian Academy of Sciences and by the National Research, Development and Innovation Office (NKFIH) under Grants PD121305, FK124256, and K125171.

REFERENCES

- Agee, E. M., 1991: Trends in cyclone and anticyclone frequency and comparison with periods of warming and cooling over the Northern Hemisphere. *J. Climate*, **4**, 263–267, [https://doi.org/10.1175/1520-0442\(1991\)004<0263:TICAAF>2.0.CO;2](https://doi.org/10.1175/1520-0442(1991)004<0263:TICAAF>2.0.CO;2).
- Budišić, M., and J.-L. Thiffeault, 2015: Finite-time braiding exponents. *Chaos*, **25**, 087407, <https://doi.org/10.1063/1.4927438>.
- Bytnerowicz, A., K. Omasa, and E. Paoletti, 2007: Integrated effects of air pollution and climate change on forests: A Northern Hemisphere perspective. *Environ. Pollut.*, **147**, 438–445, <https://doi.org/10.1016/j.envpol.2006.08.028>.
- Davis, C. A., and K. A. Emanuel, 1991: Potential vorticity diagnostics of cyclogenesis. *Mon. Wea. Rev.*, **119**, 1929–1953, [https://doi.org/10.1175/1520-0493\(1991\)119<1929:PVDOC>2.0.CO;2](https://doi.org/10.1175/1520-0493(1991)119<1929:PVDOC>2.0.CO;2).
- Dee, D., and Coauthors, 2011: The ERA-Interim reanalysis: Configuration and performance of the data assimilation system. *Quart. J. Roy. Meteor. Soc.*, **137**, 553–597, <https://doi.org/10.1002/qj.828>.
- Fang, Y., A. M. Fiore, L. W. Horowitz, A. Gnanadesikan, I. Held, G. Chen, G. Vecchi, and H. Levy, 2011: The impacts of changing transport and precipitation on pollutant distributions in a future climate. *J. Geophys. Res.*, **116**, D18303, <https://doi.org/10.1029/2011JD015642>.
- Flentje, H., and Coauthors, 2010: The Eyjafjallajökull eruption in April 2010—Detection of volcanic plume using in-situ measurements, ozone sondes and lidar-ceilometer profiles. *Atmos. Chem. Phys.*, **10**, 10085–10092, <https://doi.org/10.5194/acp-10-10085-2010>.
- Fyfe, J. C., 2003: Extratropical Southern Hemisphere cyclones: Harbingers of climate change? *J. Climate*, **16**, 2802–2805, [https://doi.org/10.1175/1520-0442\(2003\)016<2802:ESHCHO>2.0.CO;2](https://doi.org/10.1175/1520-0442(2003)016<2802:ESHCHO>2.0.CO;2).
- Geng, Q., and M. Sugi, 2001: Variability of the North Atlantic cyclone activity in winter analyzed from NCEP–NCAR reanalysis data. *J. Climate*, **14**, 3863–3873, [https://doi.org/10.1175/1520-0442\(2001\)014<3863:VOTNAC>2.0.CO;2](https://doi.org/10.1175/1520-0442(2001)014<3863:VOTNAC>2.0.CO;2).
- Graham, N. E., and H. F. Diaz, 2001: Evidence for intensification of North Pacific winter cyclones since 1948. *Bull. Amer. Meteor. Soc.*, **82**, 1869–1893, [https://doi.org/10.1175/1520-0477\(2001\)082<1869:EFIONP>2.3.CO;2](https://doi.org/10.1175/1520-0477(2001)082<1869:EFIONP>2.3.CO;2).
- Gulev, S., O. Zolina, and S. Grigoriev, 2001: Extratropical cyclone variability in the Northern Hemisphere winter from the NCEP/NCAR reanalysis data. *Climate Dyn.*, **17**, 795–809, <https://doi.org/10.1007/s003820000145>.
- Hassanzadeh, P., Z. Kuang, and B. F. Farrell, 2014: Responses of midlatitude blocks and wave amplitude to changes in the meridional temperature gradient in an idealized dry GCM. *Geophys. Res. Lett.*, **41**, 5223–5232, <https://doi.org/10.1002/2014GL060764>.
- Haszpra, T., and T. Tél, 2011: Volcanic ash in the free atmosphere: A dynamical systems approach. *J. Phys.: Conf. Ser.*, **333**, 012008, <https://doi.org/10.1088/1742-6596/333/1/012008>.
- , and —, 2013a: Escape rate: A Lagrangian measure of particle deposition from the atmosphere. *Nonlinear Processes Geophys.*, **20**, 867–881, <https://doi.org/10.5194/npg-20-867-2013>.
- , and —, 2013b: Topological entropy: A Lagrangian measure of the state of the free atmosphere. *J. Atmos. Sci.*, **70**, 4030–4040, <https://doi.org/10.1175/JAS-D-13-069.1>.
- , and A. Horányi, 2014: Some aspects of the impact of meteorological forecast uncertainties on environmental dispersion prediction. *Idojaras*, **118**, 335–347.
- , and T. Tél, 2016: Individual particle based description of atmospheric dispersion: A dynamical systems approach. *The Fluid Dynamics of Climate*, A. Provenzale, E. Palazzi, and K. Fraedrich, Eds., Springer, 95–119.
- IPCC, 2013: *Climate Change 2013: The Physical Science Basis*. Cambridge University Press, 1535 pp., <https://doi.org/10.1017/CBO9781107415324>.
- Jacob, D. J., and D. A. Winner, 2009: Effect of climate change on air quality. *Atmos. Environ.*, **43**, 51–63, <https://doi.org/10.1016/j.atmosenv.2008.09.051>.
- Kelemen, F. D., J. Bartholy, and R. Pongracz, 2015: Multivariable cyclone analysis in the Mediterranean region. *Idojaras*, **119**, 159–184.
- Kinney, P. L., 2008: Climate change, air quality, and human health. *Amer. J. Prev. Med.*, **35**, 459–467, <https://doi.org/10.1016/j.amepre.2008.08.025>.
- Lim, E.-P., and I. Simmonds, 2007: Southern Hemisphere winter extratropical cyclone characteristics and vertical organization observed with the ERA-40 data in 1979–2001. *J. Climate*, **20**, 2675–2690, <https://doi.org/10.1175/JCLI4135.1>.
- , and —, 2009: Effect of tropospheric temperature change on the zonal mean circulation and SH winter extratropical cyclones. *Climate Dyn.*, **33**, 19–32, <https://doi.org/10.1007/s00382-008-0444-0>.
- Lujanienė, G., S. Byčėnienė, P. Povinec, and M. Gera, 2012: Radionuclides from the Fukushima accident in the air over Lithuania: Measurement and modelling approaches. *J. Environ. Radioact.*, **114**, 71–80, <https://doi.org/10.1016/j.jenvrad.2011.12.004>.
- Ma, J., H. Hung, and P. Blanchard, 2004: How do climate fluctuations affect persistent organic pollutant distribution in North America? Evidence from a decade of air monitoring. *Environ. Sci. Technol.*, **38**, 2538–2543, <https://doi.org/10.1021/es0349610>.
- MacMullin, S., G. Giovanetti, M. Green, R. Henning, R. Holmes, K. Vorren, and J. F. Wilkerson, 2012: Measurement of airborne fission products in Chapel Hill, NC, USA from the Fukushima Dai-ichi reactor accident. *J. Environ. Radioact.*, **112**, 165–170, <https://doi.org/10.1016/j.jenvrad.2012.01.026>.

- McCabe, G. J., M. P. Clark, and M. C. Serreze, 2001: Trends in Northern Hemisphere surface cyclone frequency and intensity. *J. Climate*, **14**, 2763–2768, [https://doi.org/10.1175/1520-0442\(2001\)014<2763:TINHSC>2.0.CO;2](https://doi.org/10.1175/1520-0442(2001)014<2763:TINHSC>2.0.CO;2).
- Mészáros, R., Á. Leelőssy, T. Kovács, and I. Lagzi, 2016: Predictability of the dispersion of Fukushima-derived radionuclides and their homogenization in the atmosphere. *Sci. Rep.*, **6**, 19915, doi:10.1038/srep19915.
- Möller, J. D., and M. T. Montgomery, 2000: Tropical cyclone evolution via potential vorticity anomalies in a three-dimensional balance model. *J. Atmos. Sci.*, **57**, 3366–3387, [https://doi.org/10.1175/1520-0469\(2000\)057<3366:TCEVPV>2.0.CO;2](https://doi.org/10.1175/1520-0469(2000)057<3366:TCEVPV>2.0.CO;2).
- Newhouse, S., and T. Pignataro, 1993: On the estimation of topological entropy. *J. Stat. Phys.*, **72**, 1331–1351, <https://doi.org/10.1007/BF01048189>.
- Ott, E., 2002: *Chaos in Dynamical Systems*. 2nd ed. Cambridge University Press, 492 pp.
- Ottino, J., 1989: *The Kinematics of Mixing: Stretching, Chaos, and Transport*. Cambridge University Press, 364 pp.
- Serreze, M. C., F. Carse, R. G. Barry, and J. C. Rogers, 1997: Icelandic low cyclone activity: Climatological features, linkages with the NAO, and relationships with recent changes in the Northern Hemisphere circulation. *J. Climate*, **10**, 453–464, [https://doi.org/10.1175/1520-0442\(1997\)010<0453:ILCACF>2.0.CO;2](https://doi.org/10.1175/1520-0442(1997)010<0453:ILCACF>2.0.CO;2).
- Stoelinga, M. T., 1996: A potential vorticity-based study of the role of diabatic heating and friction in a numerically simulated baroclinic cyclone. *Mon. Wea. Rev.*, **124**, 849–874, [https://doi.org/10.1175/1520-0493\(1996\)124<0849:APVBSO>2.0.CO;2](https://doi.org/10.1175/1520-0493(1996)124<0849:APVBSO>2.0.CO;2).
- Tél, T., and M. Gruiz, 2006: *Chaotic Dynamics: An Introduction Based on Classical Mechanics*. Cambridge University Press, 393 pp.
- Thiffeault, J.-L., 2010: Braids of entangled particle trajectories. *Chaos*, **20**, 017516, <https://doi.org/10.1063/1.3262494>.
- Tilinina, N., S. K. Gulev, I. Rudeva, and P. Koltermann, 2013: Comparing cyclone life cycle characteristics and their interannual variability in different reanalyses. *J. Climate*, **26**, 6419–6438, <https://doi.org/10.1175/JCLI-D-12-00777.1>.
- Ulbrich, U., G. Leckebusch, and J. G. Pinto, 2009: Extra-tropical cyclones in the present and future climate: A review. *Theor. Appl. Climatol.*, **96**, 117–131, <https://doi.org/10.1007/s00704-008-0083-8>.
- Van Delden, A. J., and Y. B. L. Hinssen, 2012: PV- θ view of the zonal mean state of the atmosphere. *Tellus*, **64A**, 18710, <https://doi.org/10.3402/tellusa.v64i0.18710>.
- Wang, X. L., V. R. Swail, and F. W. Zwiers, 2006: Climatology and changes of extratropical cyclone activity: Comparison of ERA-40 with NCEP–NCAR reanalysis for 1958–2001. *J. Climate*, **19**, 3145–3166, <https://doi.org/10.1175/JCLI3781.1>.
- , Y. Feng, G. Compo, V. Swail, F. Zwiers, R. Allan, and P. Sardeshmukh, 2013: Trends and low frequency variability of extra-tropical cyclone activity in the ensemble of twentieth century reanalysis. *Climate Dyn.*, **40**, 2775–2800, <https://doi.org/10.1007/s00382-012-1450-9>.